Electron beam characterization through *K*-edge filtering of laser Compton-scattered x rays

Y. Hwang,* H. H. Effarah, T. Tajima, and C. P. J. Barty
Department of Physics and Astronomy, University of California, Irvine, Irvine, California 92967, USA

D. J. Gibson and R. A. Marsh
Lawrence Livermore National Laboratory, Livermore, California 94550, USA

(Received 9 May 2023; accepted 26 June 2023; published 17 July 2023)

A novel method of measuring an electron beam's energy spectrum and divergence using Compton-scattered x rays created by colliding a laser with an electron beam has been developed and tested using the compact laser-Compton x-ray source at LLNL. The method only requires an x-ray imaging device and a filter material whose *K*-edge energy matches that of the Compton-scattered x rays. *K*-edge filtering of energy-angle correlated Compton x rays causes large variations in intensity over the viewing angle. These intensity variations contain information about the electron beam's properties. By using simulation tools and adjusting the beam parameters to match the shape of the acquired image, the electron beam can be characterized. As a demonstration of this technique, a 75-μm Sn foil was used to filter 30-keV Compton x rays created from Compton scattering of a 532-μm laser beam by a 30-MeV electron beam. The measured parameters were mean energy $E = 28.51 \pm 0.06$ MeV, energy spread $\sigma_E < 0.3\%$, and beam divergence $\sigma_\theta = 1.8 \pm 0.1$ mrad.

DOI: 10.1103/PhysRevAccelBeams.26.072802

I. INTRODUCTION

Soon after the invention of the laser, Fiocco and Thompson observed Compton scattering of laser photons by an electron beam [1]. Since then, in addition to being studied extensively as compact light sources for hard x rays and γ rays, [2–4], photons created through the laser-Compton scattering (LCS) process have been used as diagnostics for plasmas and beams. When scattered by a relativistic electron beam, the laser photons are Doppler-shifted to very high frequencies, often in the x-ray and γ-ray regimes and highly collimated in the direction of the electron beam. Due to the strong correlation between LCS x rays and the scattering electron beam properties, LCS photons have been used to characterize almost all electron beam parameters of interest, including transverse and longitudinal beam size [5–9], divergence [8–11], energy spectrum [9–15], and polarization [16,17]. A majority of electron beam energy and divergence measurements involve measuring the spectrum of Compton x rays using conventional x- and γ-ray spectroscopy (scintillator/semiconductor single-photon counting or Bragg diffraction) and comparing the spectrum with a simulated spectrum created by an electron beam with expected parameters. Nevertheless, even if the precise measurement of the spectrum is unavailable or unfeasible, one may still be able to determine the LCS spectrum using filter attenuation methods, such as Ross filters [18,19] or attenuation through variable thickness materials [20]. An even simpler method is to use a filter material whose *K*-edge is slightly below the on-axis LCS x-ray photon energy so that the center of the x-ray beam, where the photon energy is higher, would be strongly attenuated while the outer regions are not. This method has been used to verify the energy of LCS x rays [15,21]. It is therefore logical to investigate the possibility of extending this technique to measure the electron beam parameters and compare its precision against other methods, especially spectrum-resolved LCS methods. In this paper, we present the mechanisms of our *K*-edge filtering diagnostic technique, the simulation tool, and the experimental setup and results conducted using Lawrence Livermore National Laboratory (LLNL)'s 30 MeV X-band linac to verify the technique.

II. LASER-COMPTON SCATTERING BEAM DIAGNOSTICS

A. Compton scattering from a relativistic electron

The physics of Compton scattering of laser photons by a relativistic electron or a beam of electrons has been

*yoonwooh@uci.edu

extensively studied. The two most important differences from scattering by a stationary electron are that the scattered photon is twice Doppler shifted to very high energies and that the Lorentz transform from the electron frame to the lab frame causes the scattering cross section to be highly collimated in the direction of the electron's momentum, producing a narrow beam of high energy photons. The energy E_γ of a Compton-scattered photon from a collision with a relativistic electron is

$$E_\gamma = \frac{\gamma - \sqrt{\gamma^2 - 1}\,\cos\phi}{\gamma - \sqrt{\gamma^2 - 1}\,\cos\theta + k_0 \lambda\!\!\!^{-}_c (1 - \cos\theta\,\cos\phi + \cos\psi\,\sin\theta\,\sin\phi)} E_L, \tag{1}$$

where γ is the electron's Lorentz factor, ϕ is the angle between the incident electron and the laser photon, θ is the angle between the incident electron and scattered photon, ψ is the angle between the incident and scattered photons, k_0 is the wave number of the incident photon, $\lambda\!\!\!^{-}_c$ is the reduced Compton wavelength of the electron, and E_L is the incident photon energy [22]. In the head-on collision ($\phi = \pi$) with an ultrarelativistic electron, this equation can be approximated in the small observation angles ($\theta \ll 1$) as

$$E_\gamma \approx \frac{4\gamma^2}{1 + \gamma^2\theta^2 + 4\gamma k_0 \lambda\!\!\!^{-}_c} E_L. \tag{2}$$

In this form, contributions from different components are manifest. The $4\gamma^2$ factor is due to the double Doppler upshift, while the second and third terms in the denominator represent energy reductions from the off-axis scatter and Compton recoil, respectively. The reduction in photon energy due to Compton recoil is significant only when the incident photon energy in the electron frame is comparable to the electron rest mass. As mentioned earlier, scattered light is strongly focused in the forward direction as a result of relativistic beaming. Figure 1 shows the Compton-scattered spectrum and energy-angle correlation for a 532-nm photon colliding head-on with a 25.5-MeV electron ($\gamma = 50$). It is clearly seen that the right half of the spectrum is contained within a $1/\gamma = 20$ mrad cone.

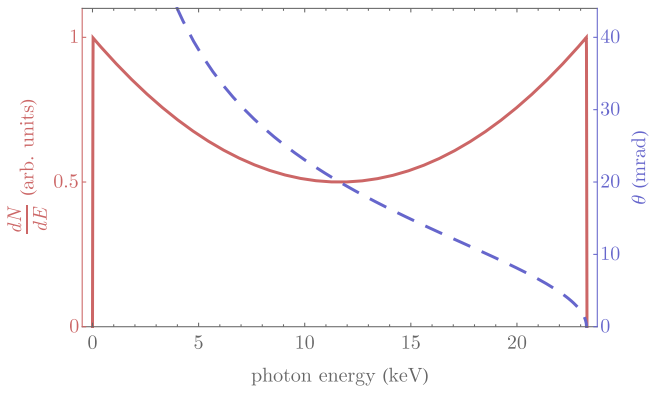

FIG. 1. Energy spectrum (solid) and scattering angle (dashed) of photons Compton-scattered from a 25.5-MeV electron ($\gamma = 50$).

B. Compton scattering from an electron beam

When a beam of electrons interacts with an intense laser, the energy-angle correlation is blurred due to multiple factors; particles traveling in different directions (divergence), particles having different energies (energy spread), multiple scattering, and nonlinear effects due to high laser intensity all contribute to the broadening of the local spectrum at a given observation angle [23–26]. Among them, the electron beam's divergence σ_θ and energy spread σ_E tend to dominate the broadening effect in typical setups where nonlinear effects are negligible and the laser bandwidth is smaller than the electron energy spread. Clearly, such reduction in coherence is detrimental in LCS light source applications; in order to control the broadening effects, much effort has been put into understanding how beam parameters affect the scattered spectrum. This knowledge can be applied backward to deduce the electron beam parameters from the LCS spectrum.

Beam divergence and energy spread affect the local spectrum in different ways [11,27–29] and is demonstrated in the simulations of x-ray spectrum in Fig. 2. Two different electron beams were simulated; a divergence-dominated beam with $\sigma_\theta = 1$ mrad and $\sigma_E = 0.06\%$, and an energy spread-dominated beam with $\sigma_\theta = 0.2$ mrad and $\sigma_E = 0.5\%$. The mean energy is 29.1 MeV for both beams. The figures on the upper half are from the divergence-dominated beam, while the ones on the lower half are from the energy spread–dominated beam. The angular-spectral distributions are shown on the left, local spectra at various detector angles θ_d are shown in the middle, and integrated spectra within various cone angles are shown on the right. The white dotted lines in the angular spectrum plots indicate the energy-angle correlation for a reference electron having $E = 29.1$ MeV and no divergence. θ_d is measured from the electron beam axis, which is antiparallel to the incident laser beam.

The shape of the local spectrum from the divergence-dominated beam, shown in Fig. 2(b), is sharp with a hard edge at the upper end for $\theta_d < 1$ mrad but becomes progressively wider further off axis. The dramatic change in bandwidth is because the energy-angle correlation is relatively flat for small angles until it takes a steep descent at around $\theta_d \approx \frac{1}{10\gamma} = 1.75$ mrad. Thus, as long as the

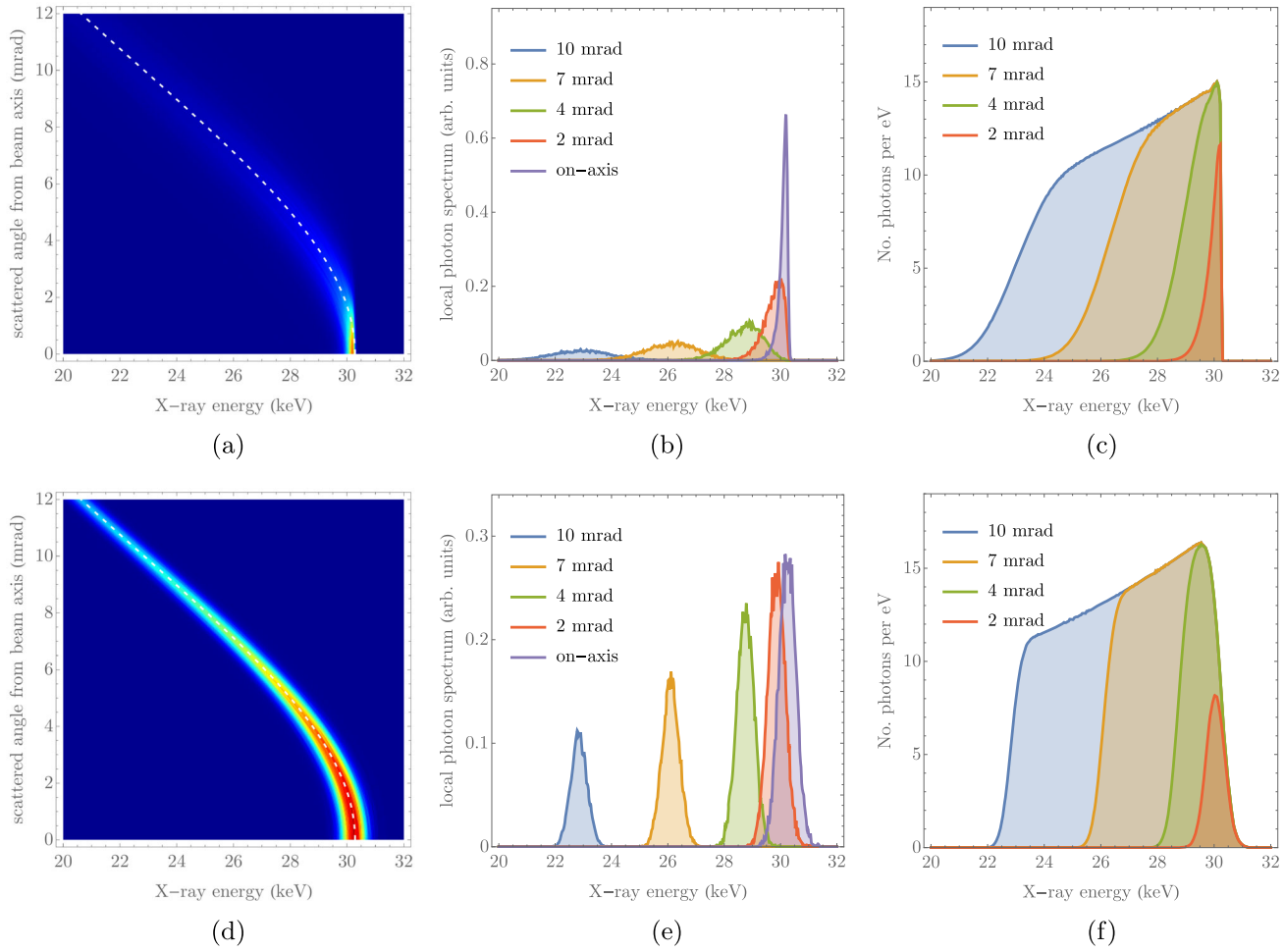

FIG. 2. Angle-resolved spectrum (a, d), local spectra (b, e), integrated spectra (c, f) for divergence-dominated beam (top) and energy spread-dominated beam (bottom). Similar analyses of spectral variation with divergence angle have been previously performed in the MeV energy regime [14,30].

divergence of the beam is less than $1/10\gamma$ as in this example, the on-axis spectrum's narrow bandwidth is preserved, while the off-axis spectrum bandwidth is greatly affected by σ_θ. One of the most distinguishing features of a divergence-dominated beam is the steep cutoff on the high-energy side of the integrated spectrum since the scattered photon energy is insensitive to small variations in laser-electron collision ϕ. In other words, the x-ray spectra from different electrons appear identical despite the difference in collision angles, only differing in direction.

On the other hand, the local spectrum from the energy spread-dominated beam is mostly a reproduction of the spectrum of the electron beam, and the shape changes very little with negligible bandwidth increase for increasing observation angles. As a result, the on-axis bandwidth is higher than that of the divergence-dominated beam, but the off-axis bandwidth is narrower, leading to a steeper cutoff at the lower end of the integrated spectrum and a gradual slope matching that of the electron energy spread at the higher end.

C. Measuring the LCS spectrum

It is clear that measuring the LCS spectrum will reveal information about the electron beam's spectrum and divergence [31] and its precision can be greatly enhanced if spectra from multiple observation points are available. Once the x-ray spectra are obtained, one can reconstruct the electron beam by simulating the Compton scattering of that beam with the laser and matching the resulting x-ray spectrum to the experimental data. Numerous experiments have measured the LCS spectra at multiple observation angles [22,32] and some have resulted in the quantitative determination of beam parameters [9–11]. Most experiments obtained the local angular spectra using single photon counting methods, either by scanning a single detector along the observation angle [10,22] or via spectroscopic imaging, where each pixel of a CCD [11] or a photodiode array [9] measures the energy of incoming photons. Bragg diffraction from crystals [32–34] has also been used to measure the angle-resolved x-ray spectra, which has several advantages over single-photon counting

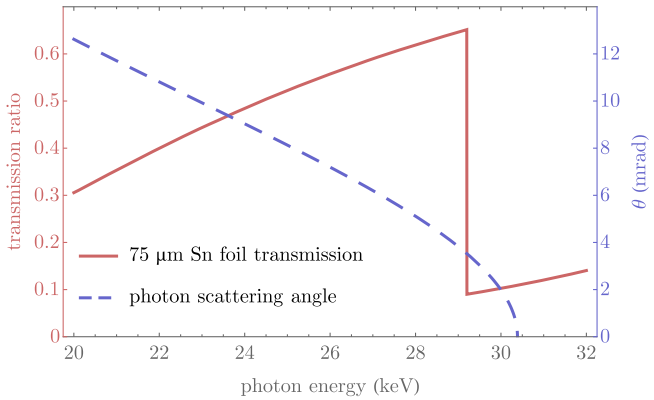

FIG. 3. X-ray transmission ratio (solid) through 75-μm thick Sn foil showing the *K*-edge at 29.2 keV and x-ray scattering angle-energy relationship (dashed, cf. Eq. (2)) from a head-on collision of 532 nm photon and 29.1 MeV electron beam which crosses the Sn *K*-edge energy at 3.4 mrad.

method since the limitation on flux due to pile-up is eliminated, and the angular spectrum is obtained in a single image. Finally, the Ross filter [35] is an established x-ray spectroscopic technique utilizing the *K*-edge absorption effect, and multiple laboratories have proposed and used the method for LCS spectroscopy [18,19]. However, the bin sizes of a Ross filter spectrometer, which are equal to differences in *K* shell edge energy of adjacent elements, are typically about 1 keV and thus too crude for the purpose of electron beam reconstruction.

III. *K*-EDGE FILTER METHOD

Brown *et al.* [15] demonstrated that filtering the LCS x-ray with a material whose *K*-edge lies slightly below the maximum energy can produce a dark spot or a "hole" in the center of the x-ray image because of the energy-angle correlation of LCS x-rays and also noticed that the sharpness of this center spot gradient depends strongly on beam divergence and energy. In that work, the maximum x-ray

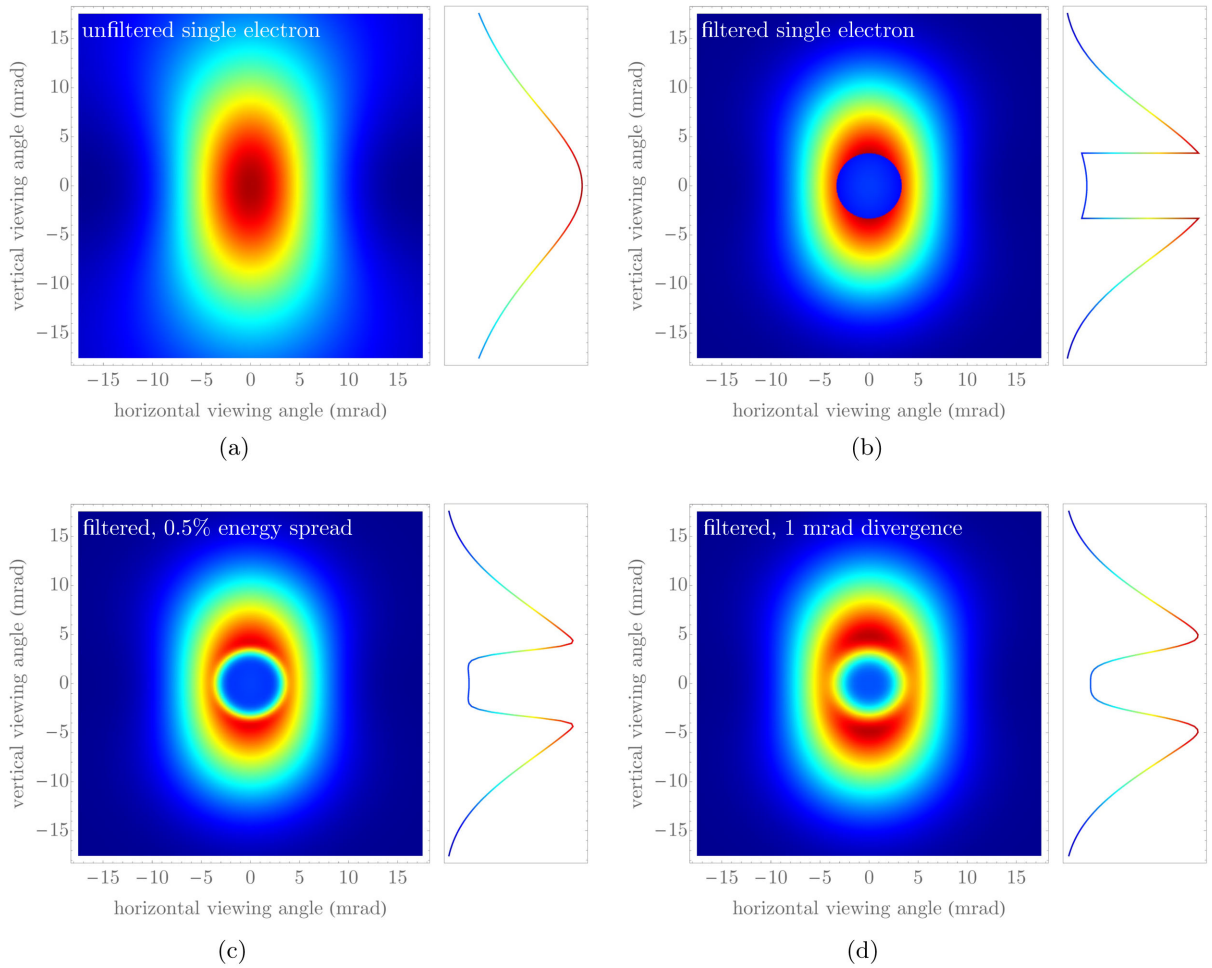

FIG. 4. (a) Compton scattering flux distribution and vertical profile through the center of a horizontally polarized 532-nm laser from a 29.1-MeV electron. (b) Flux distribution and vertical profile filtered with a 75-μm Sn foil, showing a *K*-edge hole. (c) Filtered flux distribution and vertical profile from a beam of electrons having 0.5% energy spread and no divergence. (d) Filtered flux distribution and vertical profile from a beam of electrons having 1 mrad divergence and no energy spread.

energy varied from 73 to 78 keV, and a Ta foil with a K-edge at 67 keV was used. Later, similar K-edge filter techniques were used to confirm the energy of the LCS source at BNL-ATF [21,36].

Building on the aforementioned works, we extended the K-edge hole method to measure the beam energy spread and divergence. The variation in the intensity profile of a filtered image was found to be very sensitive to the three electron beam parameters; we determined these parameters by adjusting the simulation beam parameters to match the data. In this way, one need not measure the x-ray spectrum directly; the full angular intensity distribution compensates for the lack of spectral information.

A. Beam effects on K-edge hole

A simulated image of a Compton x-ray flux distribution from a single electron is shown in Fig. 4(a). The vertical profile lineout through the center is plotted to the right. The observation angle is defined from the laser beam axis, and the electron direction is antiparallel to the laser direction. The electron's energy is 29.1 MeV, corresponding to $1/\gamma = 17.5$ mrad. The incident laser is linearly polarized in the horizontal direction which is responsible for the vertically oblong shape. With an incident laser photon wavelength of 532 nm (2.33 eV) and a head-on collision geometry, the on-axis backscattered photon energy is 30.3 keV. Figure 4(b) shows the same x rays filtered by a 75-μm thick Sn foil. The foil's attenuation spectrum and the x-ray energy-angle function are plotted in Fig. 3. A significant attenuation is visible within the central region bounded by a circle with a radius of observation angle $\theta = 3.4$ mrad, corresponding to the angle at which the scattered x-ray energy is equal to the Sn K shell energy $E_K = 29.2$ keV, and can be found by rearranging Eq. (2) for θ with E_K replacing E_γ:

$$\theta = \sqrt{\frac{4E_L}{E_K} - \frac{1}{\gamma^2} - \frac{4k_0\lambda\!\!\!^{-}_c}{\gamma}}. \tag{3}$$

The hole size is thus an indicator of electron energy given fixed laser wavelength; higher electron energy results in a larger hole. Obviously, if the maximum (on axis) scattered energy is less than the K-edge, there will be no sharp hole.

Since the sharp edge of the hole is due to the energy-angle relationship, when there is spectral broadening, the edge is softened, as some photons in the observation point will be above the K-edge while others are not. In the case of spectral broadening due to multiple electrons as discussed in Sec. II B, the softening effect can be explained as a result of a superposition of single electron-hole intensity distributions that vary in hole size and position. When the laser is scattered by a beam of electrons with nonzero energy spread, each electron contribution has a slightly different hole radius according to Eq. (3). Figure 4(c) shows the hole image when the electron beam has a 0.5% Gaussian energy spread. On the other hand, when the electron beam has nonzero divergence, each electron creates a hole centered on its own direction of travel rather than the laser-defined observation axis. Figure 4(d) shows the 3.4-mrad hole blurred due to 1-mrad Gaussian beam divergence.

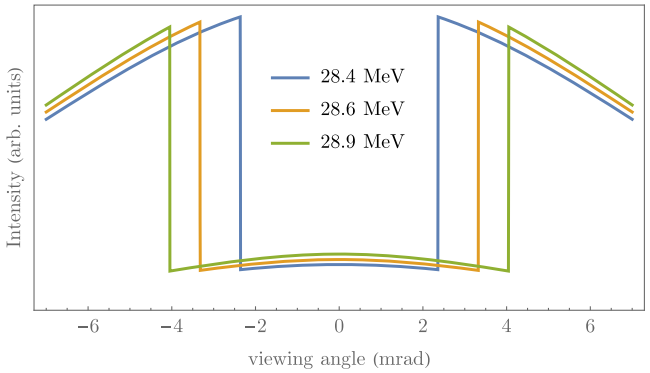

(a)

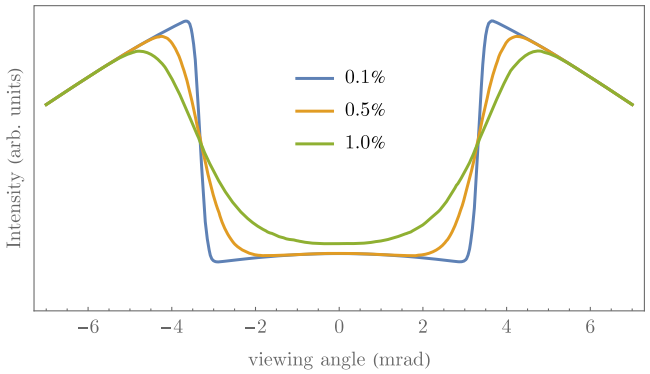

(b)

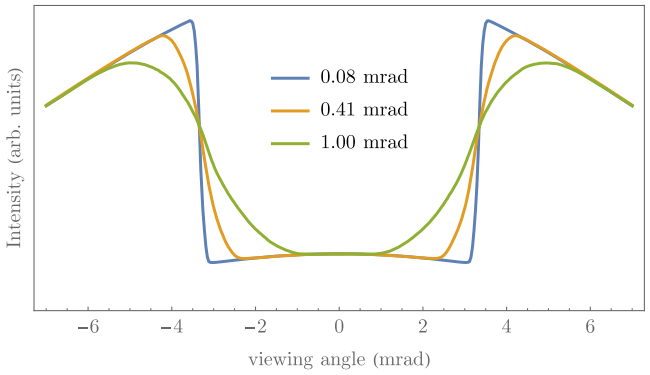

(c)

FIG. 5. Effects of different beam parameters on the K-edge hole image vertical profile: varying energy (a), varying energy spread (b), and varying divergence (c).

In the K-edge hole beam diagnostic, the beam parameters are found by first obtaining a filtered LCS x-ray image and fitting the image using simulations with ansatz beam parameters. In this demonstration, the vertical intensity profile through the center is used for checking the fit. In Fig. 5, the effects of beam parameters on the vertical profile

TABLE I. LLNL LCS source parameters.

e^- beam parameters		Laser, x-ray parameters	
Bunch charge	100 pC	Laser energy	750 mJ
Bunch length	2 ps	Pulse length	6.5 ns
Spot size	30 μm	Beam waist	50 μm
n. emittance	0.7–1.2 μm	Wavelength	532 nm
rf	11.424 GHz	X-ray energy	30 keV
Energy	30 MeV	X-ray flux	$3 \times 10^6/\mathrm{s}$
Energy spread	0.03%	Repetition rate	10 Hz

are clearly shown. Unsurprisingly, energy shift Δ_E causes the most quantifiable change by the difference in hole size. Edge blurring due to σ_E and σ_θ are more subtle, but there are important differences between the two. As mentioned before, divergence causes drastic spectral bandwidth changes along the viewing angle, while energy spread has more constant bandwidth throughout. This difference is clear when comparing the on-axis and off-axis changes. In the σ_θ case, the intensity in the central region remains unchanged as divergence increases due to the preservation of a narrow spectrum in the on-axis region, but the off-axis region is blurred considerably. Conversely, in the σ_E case, the central region gets brighter when energy spread increases to 1%, indicating the presence of more low energy photons in that area, but off-axis region slopes stay sharper than that of the $\sigma_\theta =$ 1-mrad case. These differences between energy spread and divergence are harder to distinguish when the values are small, as seen in $\sigma_E/\bar{E} = 0.5\%$ and $\sigma_\theta = 0.42$-mrad case, which is a limitation of this method in these hypothetical cases where all spectral broadening is due to either energy spread or divergence. Practically, however, independent measurements and design parameters give reasonable bounds of energy spread and divergence, which helps eliminate uncertainties. The exact shape of the slope depends on the shape of the distribution in the beam's energy spread and divergence.

IV. EXPERIMENTAL SETUP

A. Linear accelerator and interaction laser

The K-edge beam diagnostic was experimentally demonstrated using the 30-MeV X-band linear accelerator at LLNL. The accelerator was designed to produce high-brightness LCS x rays by head-on collision with a 532-nm laser. The detailed parameters of the accelerator, laser, and output x rays are given in previous publications [37–39] and summarized in Table I. Although previous publications measured a nominal normalized emittance of 0.3 μm, the measured range electron beam emittance during the time of this experiment varied between 0.7 and 1.2 μm. A layout of the laser-electron interaction region is shown in Fig. 6. The accelerated beam is focused by a quadrupole triplet just before the interaction point, where it collides head-on with the interaction laser and is bent by the spectrometer dipole to the beam dump. The energy spectrum was measured using the spectrometer, and emittance was measured using the quadrupole scanning method, showing good agreement with PARMELA design values [40,41]. For this diagnostic experiment, the energy of the electron beam was tuned so that the LCS x rays would produce a K-edge hole of adequate size given the choice of filter material and field of view. The interaction laser is linearly polarized in the horizontal direction.

B. LCS x rays

The Compton-scattered x-ray beam has a maximum energy of about 30 keV, with $1/\gamma$ divergence of 17 mrad. From the interaction region, it travels forward and passes through a 45° mirror used to direct the laser beam to the interaction region. The original thickness of the fused silica mirror is 9.525 mm, which would absorb nearly all of 30-keV x rays. In order to make it possible to image the x rays, a 20.32-mm diameter region of the mirror in its center was thinned from the back to have a 2-mm thickness. Since the mirror is positioned at 45°, the x rays penetrate through 2.828 mm of fused silica and are attenuated by about 40%; the angled position also causes this aperture region to be

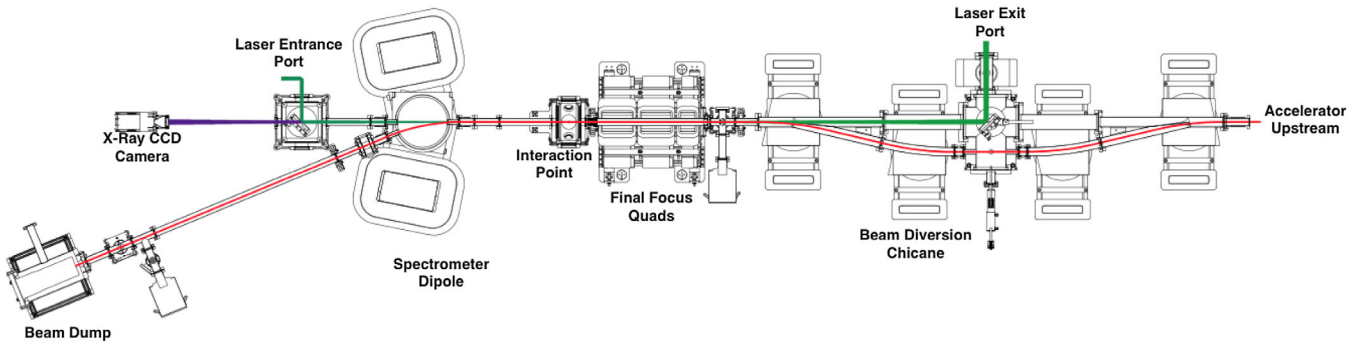

FIG. 6. Layout of the LLNL Laser-Compton Light Source interaction region and its surroundings. Electron beam path is shown in red, laser in green, and x rays in purple.

lemon shaped (vesica piscis) when imaged. The mirror is placed 1.4 m downstream of the interaction region, giving the apertured field of view of 14-mrad long and 6-mrad wide. After the mirror, the x-ray beam exits the vacuum chamber via a 435-μm thick Be window.

The x rays are then filtered by the K-edge foil. For 30-keV x rays, Sn foil was used as demonstrated in Sec. III A. For lower energies, In (27.9 keV) and Ag (25.5 keV) were used as well. The thickness of the filters was chosen to maximize the absorption difference between above and below the K-edge. For Sn, the ideal thickness is 65 μm at which the difference in absorption would be 56.6 percentage points (87.6% absorbed above K-edge, 31.0% absorbed below K-edge); 75 μm was used as it was the closest thickness available for purchase, with 56.1 p.p. difference in absorption. The filtered x rays were imaged 1.2 m further downstream with Fujifilm imaging plates and Andor image–intensified CCD cameras coupled with either a CsI scintillator or a P43 ($Gd_2O_2S:Tb$) phosphor screen. Since the CCD camera gives real-time information, it was used to monitor the centering of the x-ray beam on the aperture by steering the electron beam. However, due to an issue regarding nonuniform response across the imaging area for the CCD camera, only imaging plate data were used for analysis. The imaging plates were scanned using Fujifilm FLA-7000 within 15 min of the conclusion of exposure. Typical exposure lasted 20–30 min, corresponding to an accumulation of about 12,000–18,000 shots.

V. LASER-COMPTON X-RAY MODELING

All of the spectral and imaging simulations were done using a *Mathematica* script originally written by Hartemann and Wu for LCS optimization and modified by Yeh and Hwang. The code calculates the Compton scattering cross section and flux for a model electron beam (a collection of particles input from PARMELA) and a laser pulse modeled as a plane wave field with a Gaussian beam envelope. The original PARMELA particles' phase space values were modified to create electron beams with desired beam parameters.

In the code's coordinate system, the laser pulse is traveling along the z axis. Since it is modeled as a perfect plane wave with only intensity variations given by the Gaussian beam envelope, laser bandwidth, and divergence effects are not taken into account. A spatial grid based on observation angles θ_x and θ_y, corresponding to horizontal and vertical polar angles from the axis, respectively, serves as the 2D pixel grid. At each grid point and for each electron particle, the Compton-scattered energy and differential cross section are calculated using energy-momentum conservation and the Klein-Nishina formula for linearly polarized photons [30,42]. The interaction probability of the electron particle with the laser beam is calculated by integrating the photon density along the ballistic trajectory of the electron and is multiplied by the cross section to give the number of photons per solid angle for the grid point. This process is repeated for all grid points and electron particles and the contribution from each electron particle is summed for the final image.

The aperture created by the back-thinned optic was modeled by multiplying the cross section by the fused silica transmission coefficient with thickness depending on the expected penetration length determined from the electron particle position and the imaging grid point. Other filtration effects due to K-edge foil and Be window were calculated by simply multiplying the transmission coefficient of the respective material without added spatial complexity since the thickness is considered uniform for all x rays. Response of the imaging modality was modeled using the absorption coefficient of the respective scintillation material multiplied by the x-ray energy.

VI. RESULTS AND ANALYSIS

A 30-min (18,000 shot) integration image of unfiltered x rays captured with an imaging plate, along with a simulation of the image, is shown in Fig. 7. The horizontal and vertical profile lineouts through the center are also plotted, showing excellent agreement of intensity distribution apertured by the back-thinned optic between the experimental data and modeling.

A Sn-filtered x-ray image, also integrated for 30 min, is shown in Fig. 8 and its vertical lineout through the center and simulation fits made with varying beam parameters are

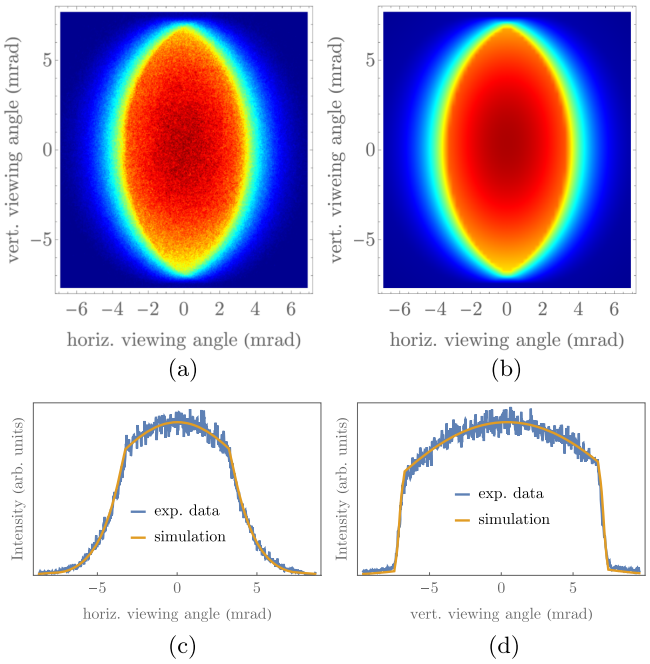

FIG. 7. Image of unfiltered x rays, apertured by the back-thinned optic (a), simulation of the unfiltered x-ray image (b), horizontal (c), and vertical (d) lineouts of the image and simulation through the center.

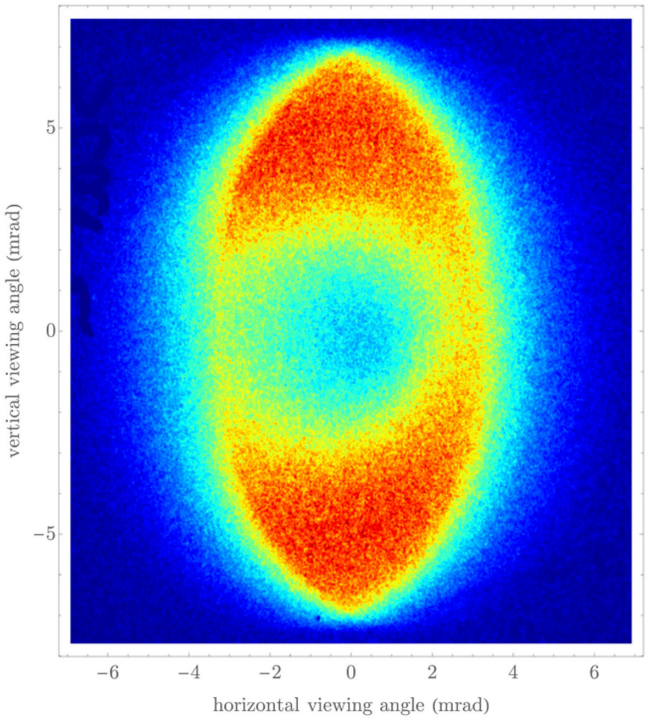

FIG. 8. Sn-filtered LCS x-ray image, showing the K-edge hole in the center.

shown in Fig. 9. The simulations were normalized to have the same intensity as the experimental data at the center and at the edges, thus easily visualizing how well the simulations fit near the shoulders for different parameters. The best-fit parameters for this image were $\bar{E} = 28.51$ MeV, $\sigma_\theta = 1.8$ mrad, and $\sigma_E/\bar{E} = 0.07\%$.

A. Mean energy

As shown in Fig. 9(a), the K-edge profile is very sensitive to the mean energy of the electron beam. The red and blue lines represent less than $\pm 0.2\%$ error in energy from best fit, plotted in purple. As expected from the ideal beam case [Fig. 5(a)], the size of the hole, measured as peak-to-peak distance, changes considerably. This method revealed a more precise measurement of energy than the spectrometer measurement where magnetic field probe calibration and angle measurement uncertainties prohibit high precision.

B. Divergence

The precision for divergence measurement is shown in Fig. 9(b). Red and blue lines represent 6% error from the best fit of 1.8 mrad. Although the typical single-shot normalized emittance of between 0.7 and 1.2 mm mrad with a 30-μm spot size implies a divergence between 0.5 and 0.8 mrad, the accumulation of 18,000 shots over 30 min seems to have introduced about a threefold increase in jitter/drift contributions to the divergence.

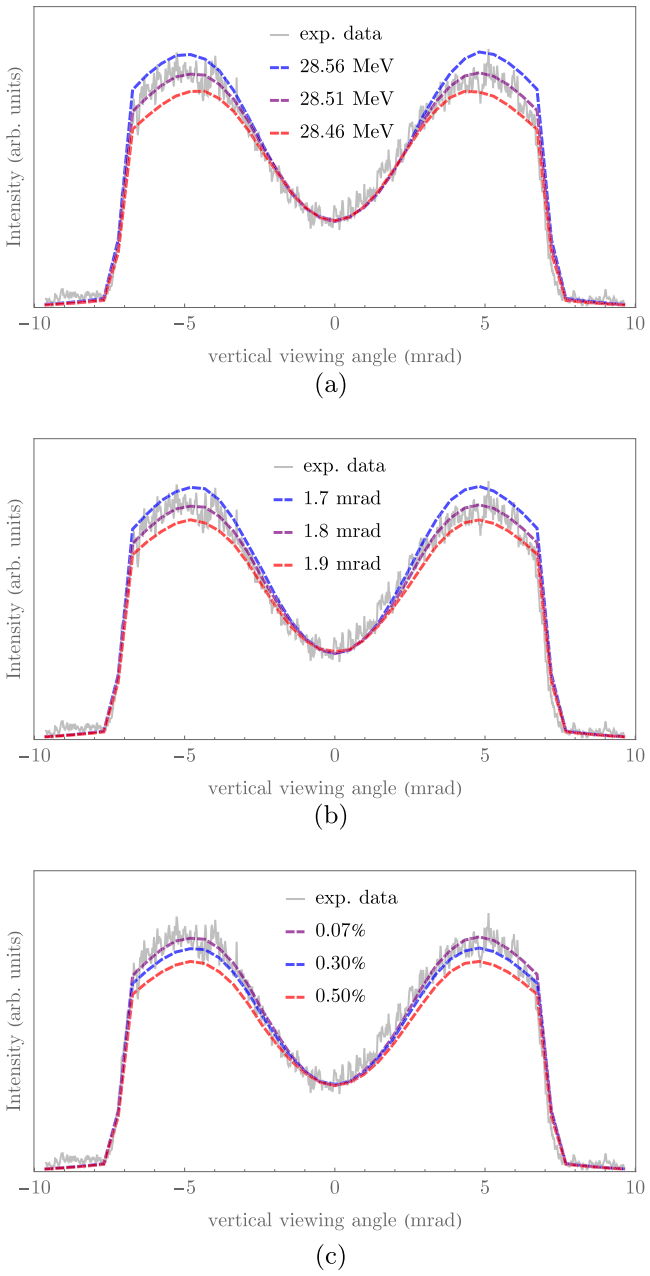

FIG. 9. Effects of different beam parameters on the K-edge hole image vertical profile: varying energy (a), varying energy spread (b), and varying divergence (c). Upper/lower bound fit errors are shown in different colors.

The possibility of the beam being energy spread-dominated with low divergence has been ruled out, as it was impossible to reproduce the exact shape with such parameters. Specifically, the profiles of high energy-spread simulations feature a flatter central trough, as explained in Sec. III A and Fig. 5.

C. Energy spread

Figure 9(c) shows the effect of changing energy spread, from nominal 0.07% in purple to 0.5% in red. Since the

beam is heavily divergence dominated, changing the energy spread value did not contribute to the off-axis spectral broadening and therefore the slope of the lineout stays unchanged within the plausible range determined from the independently measured single-shot energy spread 0.03% and jitter 0.06%. Therefore, it was only possible to give an upper bound for the energy spread at about 0.3%.

D. Applicability of the method

In this demonstration of the K-edge diagnostic, the low x-ray yield owing to the long-pulse interaction laser necessitated a half-hour integration in order to obtain a clear image and negatively affected the beam divergence measurement. With this in mind, the K-edge diagnostic is best suited for sources with high x-ray flux. For example, this method would be most ideal for measuring the single shot beam emittance of laser wakefield accelerator beams, as such facilities already possess high-intensity lasers capable of producing bright LCS x rays and divergence measurement options are limited [9]. The energy spectrum as measured from the dipole spectrometer supplies the spectral broadening contribution due to the energy spread, so simulating the x rays only requires making ansatz divergence distributions. It should be noted that high intensity lasers commonly used to drive plasma wakefield will introduce nonlinear effects that also contribute to spectral broadening and must be accounted for in the simulations.

The choice of filter material should be made based on the energy range of the electron beam and the laser wavelength; since there is an upper limit on atomic absorption edges—Pu K-edge is 121 keV—if the electron beam energy is too high, the LCS x-ray energy can be lowered by using a longer wavelength laser or reducing the interaction angle. Additionally, in cases where both electron beam energy and divergence are high enough that $1/\gamma$ divergence of the LCS x rays is smaller than the beam divergence, the K-edge hole would be very difficult to image. Therefore, this method is best suited for energies below 100 MeV, where the LCS divergence would be wide enough for imaging the hole, and filter materials are commonly available.

VII. CONCLUSION

A diagnostic method that can determine the electron beam's energy spectrum and divergence using K-edge filter imaging of LCS x rays has been developed and tested on the X-band linear accelerator at LLNL. K-edge foils act as low-pass filters attenuating most of the x rays above the K-edge energy; the LCS spectral broadening due to beam divergence and energy spread is rendered as a gradual slope from dark, high energy region in the center to bright low energy region off-axis. By finding the beam parameters that fit the shape of the slope, one can determine the mean energy, energy spread, and divergence. The 30-keV LCS x rays were filtered with 29.2-keV Sn K-edge foil and were able to find the mean energy and divergence with high precision. Because the spectral broadening was dominated by the divergence, only an upper limit for the energy spread could be obtained. Due to the precise divergence measurement capability, this method can be a very simple yet useful emittance measurement tool when combined with a spot size measurement for moderate energy electron beams.

ACKNOWLEDGMENTS

The authors are indebted to F. V. Hartemann and S. Wu for code troubleshooting, F. Albert for providing the imaging plates, S. M. Betts and G. G. Anderson for experimental support and troubleshooting. This work was performed under the auspices of the U.S. Department of Energy by Lawrence Livermore National Laboratory under Contract No. DE-AC52-07NA27344. This work was in part supported by the Norman Rostoker Fund.

[1] G. Fiocco and E. Thompson, Phys. Rev. Lett. **10**, 89 (1963).
[2] P. Sprangle, A. Ting, E. Esarey, and A. Fisher, J. Appl. Phys. **72**, 5032 (1992).
[3] M. Fujiwara, K. Kawase, and A. T. Titov, AIP Conf. Proc. **802**, 246 (2005).
[4] G. A. Mourou, T. Tajima, and S. V. Bulanov, Rev. Mod. Phys. **78**, 309 (2006).
[5] T. Shintake, Nucl. Instrum. Methods Phys. Res., Sect. A **311**, 453 (1992).
[6] V. Balakin *et al.*, Phys. Rev. Lett. **74**, 2479 (1995).
[7] R. Alley, D. Arnett, E. Bong, W. Colocho, J. Frisch, S. Horton-Smith, W. Inman, K. Jobe, T. Kotseroglou, D. McCormick, J. Nelson, M. Scheeff, S. Wagner, and M. Ross, Nucl. Instrum. Methods Phys. Res., Sect. A **379**, 363 (1996).
[8] W. P. Leemans, R. W. Schoenlein, P. Volfbeyn, A. H. Chin, T. E. Glover, P. Balling, M. Zolotorev, K. J. Kim, S. Chattopadhyay, and C. V. Shank, Phys. Rev. Lett. **77**, 4182 (1996).
[9] G. Golovin, S. Banerjee, C. Liu, S. Chen, J. Zhang, B. Zhao, P. Zhang, M. Veale, M. Wilson, P. Seller, and D. Umstadter, Sci. Rep. **6**, 24622 (2016).
[10] K. Chouffani, F. Harmon, D. Wells, J. Jones, and G. Lancaster, Phys. Rev. ST Accel. Beams **9**, 050701 (2006).
[11] A. Jochmann, A. Irman, M. Bussmann, J. P. Couperus, T. E. Cowan, A. D. Debus, M. Kuntzsch, K. W. D. Ledingham, U. Lehnert, R. Sauerbrey, H. P. Schlenvoigt, D. Seipt, T. Stöhlker, D. B. Thorn, S. Trotsenko, A. Wagner, and U. Schramm, Phys. Rev. Lett. **111**, 114803 (2013).
[12] H. Ohgaki, S. Sugiyama, T. Yamazaki, T. Mikado, M. Chiwaki, K. Yamada, R. Suzuki, T. Noguchi, and T. Tomimasu, IEEE Trans. Nucl. Sci. **38**, 386 (1991).
[13] R. Klein, T. Mayer, P. Kuske, R. Thornagel, and G. Ulm, Nucl. Instrum. Methods Phys. Res., Sect. A **384**, 293 (1997).

[14] C. Sun, J. Li, G. Rusev, A. P. Tonchev, and Y. K. Wu, Phys. Rev. ST Accel. Beams **12**, 062801 (2009).

[15] W. J. Brown, S. G. Anderson, C. P. J. Barty, S. M. Betts, R. Booth, J. K. Crane, R. R. Cross, D. N. Fittinghoff, D. J. Gibson, F. V. Hartemann, E. P. Hartouni, J. Kuba, G. P. Le Sage, D. R. Slaughter, A. M. Tremaine, A. J. Wootton, P. T. Springer, and J. B. Rosenzweig, Phys. Rev. ST Accel. Beams **7**, 060702 (2004).

[16] V. N. Baier and V. A. Khoze, Sov. J. Nucl. Phys. **9**, 238 (1969), https://inspirehep.net/literature/54843.

[17] D. Gustavson, J. Murray, T. Phillips, R. Schwitters, C. Sinclair, J. Johnson, R. Prepost, and D. Wiser, Nucl. Instrum. Methods **165**, 177 (1979).

[18] P. Cardarelli, G. D. Domenico, M. Marziani, I. Muçollari, G. Pupillo, F. Sisini, A. Taibi, and M. Gambaccini, J. Appl. Phys. **112**, 074908 (2012).

[19] N. D. Powers, I. Ghebregziabher, G. Golovin, C. Liu, S. Chen, S. Banerjee, J. Zhang, and D. P. Umstadter, Nat. Photonics **8**, 28 (2014).

[20] F. V. Hartemann, A. M. Tremaine, S. G. Anderson, C. P. J. Barty, S. M. Betts, R. Booth, W. J. Brown, J. K. Crane, R. R. Cross, D. J. Gibson, D. N. Fittinghoff, J. Kuba, G. P. Le Sage, D. R. Slaughter, A. J. Wootton, E. P. Hartouni, P. T. Springer, J. B. Rosenzweig, and A. K. Kerman, Laser Part. Beams **22**, 221 (2004).

[21] O. Williams, G. Andonian, M. Babzien, E. Hemsing, K. Kusche, J. Park, I. Pogorelsky, G. Priebe, J. Rosenzweig, and V. Yakimenko, Nucl. Instrum. Methods Phys. Res., Sect. A **608**, S18 (2009).

[22] F. Albert, S. G. Anderson, D. J. Gibson, C. A. Hagmann, M. S. Johnson, M. Messerly, V. Semenov, M. Y. Shverdin, B. Rusnak, A. M. Tremaine, F. V. Hartemann, C. W. Siders, D. P. McNabb, and C. P. J. Barty, Phys. Rev. ST Accel. Beams **13**, 070704 (2010).

[23] C. Bula, K. T. McDonald, E. J. Prebys, C. Bamber, S. Boege, T. Kotseroglou, A. C. Melissinos, D. D. Meyerhofer, W. Ragg, D. L. Burke, R. C. Field, G. Horton-Smith, A. C. Odian, J. E. Spencer, D. Walz, S. C. Berridge, W. M. Bugg, K. Shmakov, and A. W. Weidemann, Phys. Rev. Lett. **76**, 3116 (1996).

[24] C. A. Brau, Phys. Rev. ST Accel. Beams **7**, 020701 (2004).

[25] G. A. Krafft, Phys. Rev. Lett. **92**, 204802 (2004).

[26] F. V. Hartemann, W. J. Brown, D. J. Gibson, S. G. Anderson, A. M. Tremaine, P. T. Springer, A. J. Wootton, E. P. Hartouni, and C. P. J. Barty, Phys. Rev. ST Accel. Beams **8**, 100702 (2005).

[27] S. G. Rykovanov, C. G. R. Geddes, J.-L. Vay, C. B. Schroeder, E. Esarey, and W. P. Leemans, J. Phys. B **47**, 234013 (2014).

[28] C. Curatolo, I. Drebot, V. Petrillo, and L. Serafini, Phys. Rev. Accel. Beams **20**, 080701 (2017).

[29] N. Ranjan, B. Terzić, G. Krafft, V. Petrillo, I. Drebot, and L. Serafini, Phys. Rev. Accel. Beams **21**, 030701 (2018),

[30] G. Krafft, E. Johnson, K. Deitrick, B. Terzić, R. Kelmar, T. Hodges, W. Melnitchouk, and J. Delayen, Phys. Rev. Accel. Beams **19**, 121302 (2016).

[31] A. Jochmann, A. Irman, U. Lehnert, J. Couperus, M. Kuntzsch, S. Trotsenko, A. Wagner, A. Debus, H.-P. Schlenvoigt, U. Helbig, S. Bock, K. Ledingham, T. Cowan, R. Sauerbrey, and U. Schramm, Nucl. Instrum. Methods Phys. Res., Sect. B **309**, 214 (2013).

[32] Z. Chi, L. Yan, Z. Zhang, Z. Zhou, L. Zheng, D. Wang, Q. Tian, W. Wang, Z. Nie, J. Zhang, Y. Du, J. Hua, J. Shi, C. Pai, W. Lu, W. Huang, H. Chen, and C. Tang, Rev. Sci. Instrum. **88**, 045110 (2017).

[33] F. H. O'Shea, O. Williams, G. Andonian, S. Barber, Y. Sakai, J. B. Rosenzweig, I. Pogorelsky, M. Fedurin, K. Kusche, and V. Yakimenko, Phys. Rev. ST Accel. Beams **15**, 020702 (2012).

[34] Y. Sakai *et al.*, Phys. Rev. Accel. Beams **20**, 060701 (2017).

[35] P. A. Ross, J. Opt. Soc. Am. **16**, 433 (1928).

[36] Y. Sakai, I. Pogorelsky, O. Williams, F. O'Shea, S. Barber, I. Gadjev, J. Duris, P. Musumeci, M. Fedurin, A. Korostyshevsky, B. Malone, C. Swinson, G. Stenby, K. Kusche, M. Babzien, M. Montemagno, P. Jacob, Z. Zhong, M. Polyanskiy, V. Yakimenko, and J. Rosenzweig, Phys. Rev. ST Accel. Beams **18**, 060702 (2015).

[37] R. Marsh, G. Anderson, C. Barty, D. Gibson, and Y. Hwang, in *Proceedings of 7th International Particle Accelerator Conference (IPAC'16), Busan, Korea, 2016* (JACoW, Geneva, Switzerland, 2016) pp. 3993–3995, 10.18429/JACoW-IPAC2016-THPOW026.

[38] Y. Hwang, G. Anderson, C. Barty, D. Gibson, R. Marsh, and T. Tajima, in *Proceedings of International Particle Accelerator Conference (IPAC'16), Busan, Korea, May 8-13, 2016*, International Particle Accelerator Conference No. 7 (JACoW, Geneva, Switzerland, 2016), pp. 1885–1888, 10.18429/JACoW-IPAC2016-TUPOW052.

[39] Y. Hwang, G. Anderson, C. Barty, D. Gibson, R. Marsh, and T. Tajima, in *Proceedings of 3rd North American Particle Accelerator Conference (NAPAC'16), Chicago, IL, 2016* (JACoW, Geneva, Switzerland, 2017), pp. 977–979, 10.18429/JACoW-NAPAC2016-WEPOB35.

[40] R. A. Marsh *et al.*, Phys. Rev. ST Accel. Beams **15**, 102001 (2012).

[41] R. A. Marsh, G. G. Anderson, S. G. Anderson, D. J. Gibson, C. P. J. Barty, and Y. Hwang, Performance of a second generation x-band rf photoinjector, Phys. Rev. Accel. Beams **21**, 073401 (2018).

[42] G. Bhatt, H. Grotch, E. Kazes, and D. A. Owen, Phys. Rev. A **28**, 2195 (1983).